

Optimization of a Common Buffer Platform for Monolithic Integration of InGaN/GaN Light-Emitting Diodes and AlGaIn/GaN High-Electron-Mobility Transistors

CHAO LIU,¹ YUEFEI CAI,¹ HUAXING JIANG,¹ and KEI MAY LAU^{1,2}

1.—Photonics Technology Center, Department of Electronic and Computer Engineering, Hong Kong University of Science and Technology, Clear Water Bay, Kowloon, Hong Kong. 2.—e-mail: eekmlau@ust.hk

For the development of a metal-interconnection-free integration scheme for monolithic integration of InGaN/GaN light-emitting diodes (LEDs) and AlGaIn/GaN high-electron-mobility transistors (HEMTs), a common buffer to achieve high brightness, low leakage current, and high breakdown in the integrated HEMT–LED device is essential. Different buffer structures have been investigated, and their impacts upon both the LED and HEMT parts of the HEMT–LED device have been analyzed. Results indicated that a GaN/AlN buffer structure is the most ideal to serve as a common buffer platform, offering both the excellent crystalline quality and superior buffer resistivity required by the HEMT–LED device. Growth of the AlN layer was particularly crucial for engineering the dislocation density, surface morphology, as well as resistivity of the buffer layer. Using the optimized GaN/AlN buffer structure, the LED part of the HEMT–LED device was improved, showing greatly enhanced light output power and suppressed reverse leakage current, while the breakdown characteristics of the HEMT part were also improved.

Key words: Metalorganic chemical vapor deposition, light-emitting diodes, high-electron-mobility transistors, HEMT–LED integration

INTRODUCTION

Integration of InGaN/GaN light-emitting diodes (LEDs) and AlGaIn/GaN high-electron-mobility transistors (HEMTs) on a common material platform is attracting interest due to its advantages in reducing device footprint, enhancing system reliability, and minimizing interconnect-related parasitics.¹ To accomplish a monolithically integrated HEMT–LED device, a few different schemes have been reported, including selective epi removal (SER), selective epitaxial growth (SEG), and wafer bonding techniques.^{2–8} Recently, we demonstrated a metal-interconnection-free scheme for HEMT–LED integration by combining SER and SEG procedures. A schematic of the monolithically integrated HEMT–LED structure is shown in Fig. 1. Key to this method

is obtaining intimate and seamless contact between the GaN channel of the HEMT and the *n*-type layer of the LED. Effective modulation of the LED brightness by gate control of the driving current injected through the HEMT has been demonstrated.⁹ However, due to the difference in material requirements for the LED and HEMT, it is not trivial to achieve high brightness in the LED part and high breakdown in the HEMT part simultaneously. A common buffer platform with both high crystalline quality and high resistivity for the monolithically integrated HEMT–LED device that can lead to this goal is therefore highly desirable.

In early studies, a two-step growth procedure using low-temperature GaN (LT-GaN) as nucleation layer was typically used to promote two-dimensional (2D) GaN growth on sapphire.¹⁰ Afterwards, several groups demonstrated that an intentionally prolonged three-dimensional (3D) growth mode in the early stage of GaN growth could effectively reduce the

(Received August 20, 2015; accepted February 3, 2016; published online February 18, 2016)

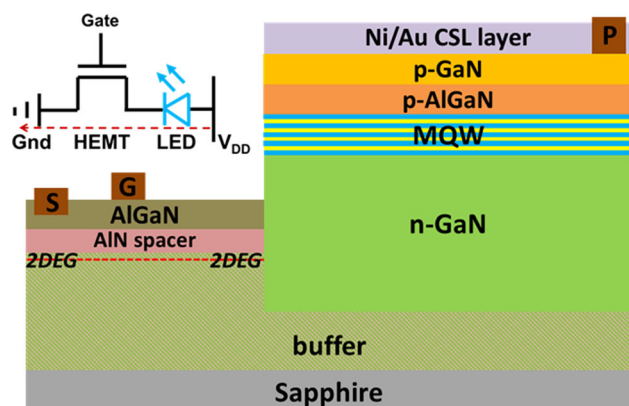


Fig. 1. Schematic of monolithically integrated HEMT-LED structure using metal-interconnection-free integration scheme.

threading dislocation density and improve the crystalline quality,^{11,12} boosting the performance of GaN-based light-emitting diodes. However, it was recently found that the 3D growth mode was accompanied by enhanced unintentional doping that introduces a buried conductive channel and degrades the buffer breakdown,^{13,14} being the most undesirable characteristics for transistors. Although acceptor-like impurities (e.g., Fe, Mg) can be introduced to compensate the background donor states and enhance the resistivity of the GaN buffer layer,^{15–18} Mg and Fe are known to have serious memory effects,^{16,17} potentially redistributing towards the channel region and degrading device performance. A high-resistivity buffer without compensating dopants that also eliminates the conductive channel induced by the 3D growth mode¹⁹ would be most ideal. The alternative of GaN buffers on sapphire using AlN as nucleation layer would not introduce leaky channels and could potentially provide high crystalline quality and high buffer resistivity simultaneously.^{20–24} However, growth of this kind of GaN buffers occurs in a narrow growth window. The best crystalline quality and surface morphology can only be achieved when neither Al nor N atoms dominate at the surface.^{25,26}

To optimize the integrated HEMT-LED performance, we have developed a GaN/AlN buffer platform featuring high buffer resistivity and excellent crystalline quality simultaneously. The influence of the growth temperature and the V/III ratio of the AlN layer on the crystalline quality and surface morphology of the upper AlGaIn/GaN heterostructures has been investigated. Under optimal AlN growth conditions, the dislocation density in the GaN buffer can be reduced to $3.2 \times 10^8 \text{ cm}^{-2}$ with high resistivity. To verify the advantages of the GaN/AlN buffer structure, we studied the effect of different buffer structures on the performance of the HEMT and LED parts of the HEMT-LED device. Based on the high-quality GaN/AlN buffer, improved light output power and suppressed reverse leakage current were achieved in the LED

part. Meanwhile, low buffer leakage was achieved. Therefore, the GaN/AlN buffer structure developed in this work is promising to serve as a common platform for HEMT-LED integration.

EXPERIMENTAL PROCEDURES

This study was carried out using a previously proven scheme for the integrated device.⁹ The AlGaIn/GaN HEMT structures used in this work were grown on 2-inch sapphire substrates in an Aixtron 2400HT metalorganic chemical vapor deposition (MOCVD) system. Trimethylgallium (TMGa), trimethylaluminum (TMAI), and ammonia (NH_3) were used as Ga, Al, and N source, respectively. Nitrogen and hydrogen were used as carrier gas. Three buffer structures were used for AlGaIn/GaN HEMT growth in this work, as shown in Fig. 2. With different temperature ramping rates and parameters for the initial high-temperature GaN growth, high-quality (HQ) and high-resistivity (HR) GaN buffers on sapphire can be achieved, respectively, as shown in Fig. 2a and b. The HQ GaN buffer was grown using the method widely adopted for growing LEDs on sapphire. A 25-nm GaN nucleation layer was deposited at 550°C , followed by temperature ramping to 1150°C in 7 min and *in situ* annealing for 2 min. During the annealing, small grains start to decompose, leaving a low density of large grains. This was followed by high-temperature GaN buffer growth at 200 mbar. Three-dimensional (3D) grain growth first occurs on the island-like grains of the nucleation layer prior to the two-dimensional (2D) coalesced growth. The 3D-to-2D transition growth mode was accompanied with epitaxial lateral overgrowth (ELOG), which can effectively reduce the threading dislocation density. Meanwhile, for HR GaN buffer growth, the reactor temperature was ramped up to 1050°C in 3 min after low-temperature GaN nucleation, followed by immediate growth of high-temperature GaN at 50 mbar. The increased temperature ramping rate without annealing helped to maintain a quasi-2D morphology for the low-temperature GaN nucleation layer. Moreover, the lower reactor pressure can ensure direct 2D growth for the high-temperature GaN. As a result, unintentional doping during the 3D growth can be avoided and the leakage channel at the sapphire-GaN interface eliminated.

Alternatively, AlGaIn/GaN HEMTs using GaN/AlN buffer were also investigated, as shown in Fig. 2c. To optimize the GaN/AlN buffer for HEMT applications, a series of growth experiments were carried out. With the thickness of the AlN nucleation layer kept at 150 nm, the growth conditions of the AlN layer for five samples were varied as listed in Table I. The reactor pressure was fixed at 50 mbar for all samples. Samples A to C were used to observe the effects of growth temperature, while samples C to E were used to observe the effects of

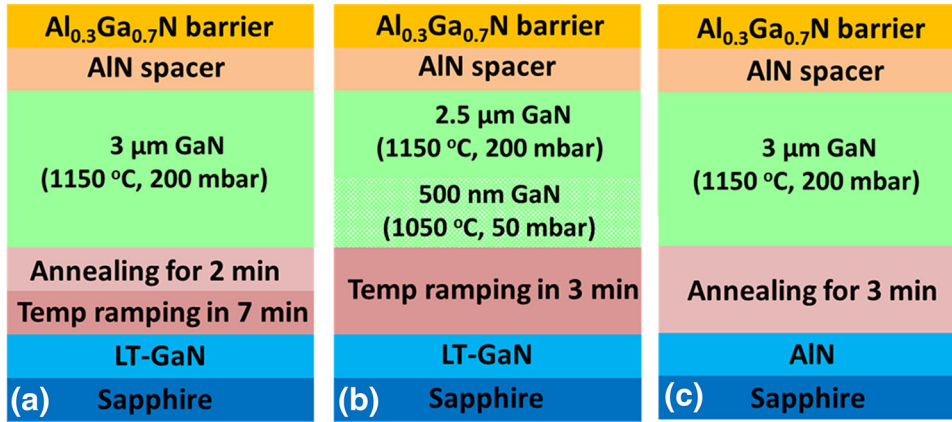


Fig. 2. Schematic of AlGaIn/GaN HEMTs using different buffer structures: (a) high quality (HQ) GaN buffer, (b) high-resistivity (HR) GaN buffer, and (c) GaN/AlN buffer.

Table I. Growth parameters of AlN buffer for AlGaIn/GaN HEMTs on sapphire

Sample	Temperature (°C)	Pressure (hPa)	NH ₃ Flow Rate (mmol/min)	TMAI Flow Rate (μmol/min)	V/III
A	950	50	22	40	550
B	1050	50	22	40	550
C	1150	50	22	40	550
D	1150	50	9	40	225
E	1150	50	45	40	1000

the V/III ratio during AlN growth. Atomic force microscopy (AFM) and high-resolution x-ray diffraction (HRXRD) were used to characterize the surface morphology and crystalline quality of the as-grown AlGaIn/GaN HEMT epi on top. Mercury capacitance–voltage (*C*–*V*) probe measurements were implemented to determine the background carrier concentration and monitor the leakage channel in the buffer layer. The electron transport properties of the AlGaIn/GaN HEMT epi were investigated by van der Pauw–Hall measurements, using ohmic contacts formed by alloyed indium dots on the AlGaIn barrier. Afterwards, the AlGaIn/GaN stack was selectively removed by inductively coupled plasma (ICP) etching, exposing the GaN buffer underneath for subsequent LED overgrowth. The overgrown LED structure consisted of 1.5-μm *n*-type GaN, five periods of In_{0.1}Ga_{0.9}N/GaN multi quantum wells (MQWs) with 3-nm-thick wells and 12-nm-thick barriers, followed by a 15-nm *p*-type Al_{0.15}Ga_{0.85}N and a 170-nm *p*-type GaN layer. After the growth, both discrete LEDs and integrated HEMT–LEDs were fabricated. Details of the fabrication process can be found in Ref. 9. Electrical properties were measured by on-wafer probing, and luminescence properties were collected using a calibrated integrating sphere at room temperature.

RESULTS AND DISCUSSION

Figure 3a, b, and c show the surface morphologies of the AlGaIn/GaN HEMTs grown on GaN/AlN

buffers with AlN deposited at 950°C, 1050°C, and 1150°C, respectively (labeled sample A, B, and C, respectively). Fragmented surface morphology with large and deep pits can be observed for sample A. This is due to incomplete coalescence of the initial 3D AlN islands at low temperature. When the AlN temperature was increased to 1050°C in sample B, step-flow morphology can be observed on the final AlGaIn/GaN surface, with root-mean-square (RMS) roughness decreased from 4.5 nm to 0.8 nm. The associated large density of surface pits lowers the effective barrier height and increases the reverse gate leakage current of the fabricated HEMT devices.²⁷ When the AlN temperature was further increased to 1150°C, sample C showed a pit-free surface with RMS roughness of 0.3 nm, which can be attributed to the enhanced Al atom mobility at higher temperature.

In addition to the AlN growth temperature, the V/III ratio of the AlN layer also plays an important role in the surface morphologies of the upper AlGaIn/GaN HEMTs. It is well known that inversion domains can form during AlN growth if there is prereaction between NH₃ and Al₂O₃, causing mixed domains and thus rough surface.²⁸ TMAI preflow presumably helps to eliminate the inversion domain problem. However, alumination of the sapphire surface results in much larger tilt of the AlN nuclei, degrading the crystalline quality, as indicated by an increase of the GaN XRD peak full-width at half-maximum (FWHM).²⁹ In this work, no TMAI

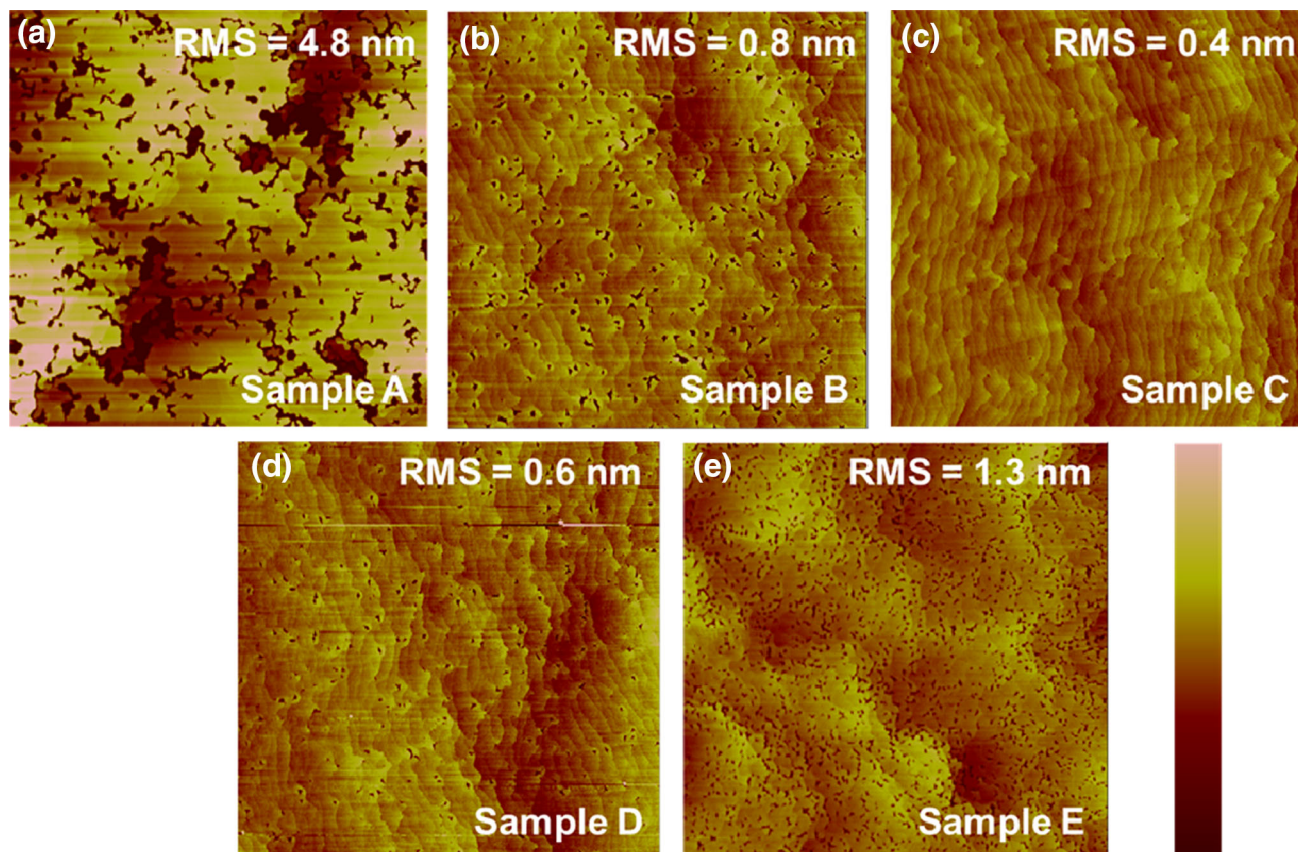


Fig. 3. Surface morphology of samples A to E, with different AlN growth conditions. All scans are $5 \mu\text{m} \times 5 \mu\text{m}$; vertical scale bars are 15 nm, 5 nm, 5 nm, 5 nm, and 10 nm for samples A to E, respectively (Color figure online).

preflow was used, but optimizing the ammonia flow at high temperature was found to be effective. Figure 3c–e depicts the dependence of the surface morphology on the V/III ratio of the AlN layer at fixed growth temperature of 1150°C and reactor pressure of 50 mbar. The lowest density of surface pits on the AlGaN/GaN HEMT surface was obtained with a V/III ratio of 550 (sample C). The pinholes may be either attributed to inversion domains or due to threading dislocations that terminate at the sample surface.³⁰

The dependence of the crystalline quality and surface roughness of the AlGaN/GaN/AlN heterostructures on the growth temperature and V/III ratio of the AlN layer is plotted in Fig. 4. The FWHM value of the GaN/AlN buffer decreased monotonically with increased AlN growth temperature, whereby enhanced Al atom mobility can lead to reduced misorientations and nuclei density in the AlN layer. As a result, fewer threading dislocations can penetrate into the upper GaN buffer, and improved crystalline quality can be achieved. This phenomenon agrees with the results reported by Li et al.³¹ The V/III ratio of the AlN layer growth also affects the crystalline quality of the upper GaN buffer, with a minimal FWHM value at V/III ratio of 500. Furthermore, it is worth noting that the

surface roughness and XRD linewidth exhibited similar trends with growth temperature. This coincidence indicates that, with reduced misorientations and nuclei densities of the initial AlN nuclei under the optimal AlN growth condition, reduced surface roughness and improved crystalline quality can be achieved simultaneously.

Using the optimum AlN growth condition described above, an AlGaN/GaN HEMT structure was grown using the GaN/AlN buffer structure, to be compared with two other HEMT samples grown using conventional HQ GaN buffer and HR GaN buffer, respectively. The surface morphologies of the as-grown AlGaN/GaN HEMT epi on different buffer structures were compared by AFM (Fig. 5). Well-aligned step flow could be observed for the HEMT on the HQ GaN buffer, with an RMS value of 0.4 nm. The RMS value of the AlGaN/GaN surface with HR GaN buffer increased to 0.6 nm, accompanied by disordered step flow, due to increased misorientations and nuclei density of the GaN nucleation layer by eliminating the 3D-to-2D transition growth mode. The AlGaN/GaN heterostructure on the GaN/AlN buffer also exhibited a well-aligned surface with an RMS value as small as 0.3 nm. The surface morphology is one of the vital factors influencing the transport properties of the

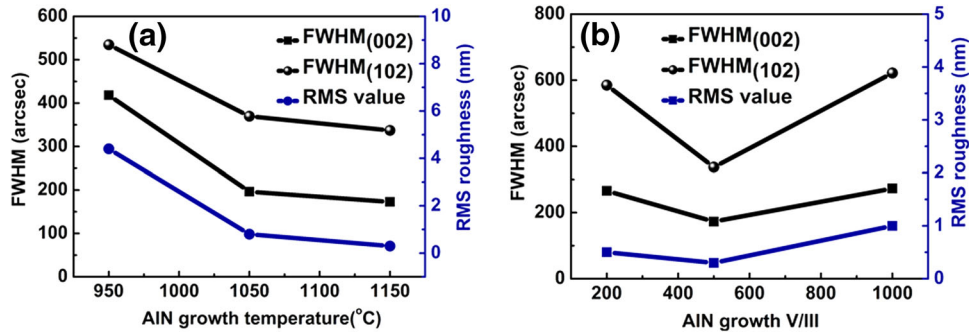


Fig. 4. Dependence of crystalline quality and surface roughness of AlGaIn/GaN/AlIn heterostructures on (a) AlIn growth temperature and (b) V/III ratio of AlIn layer (Color figure online).

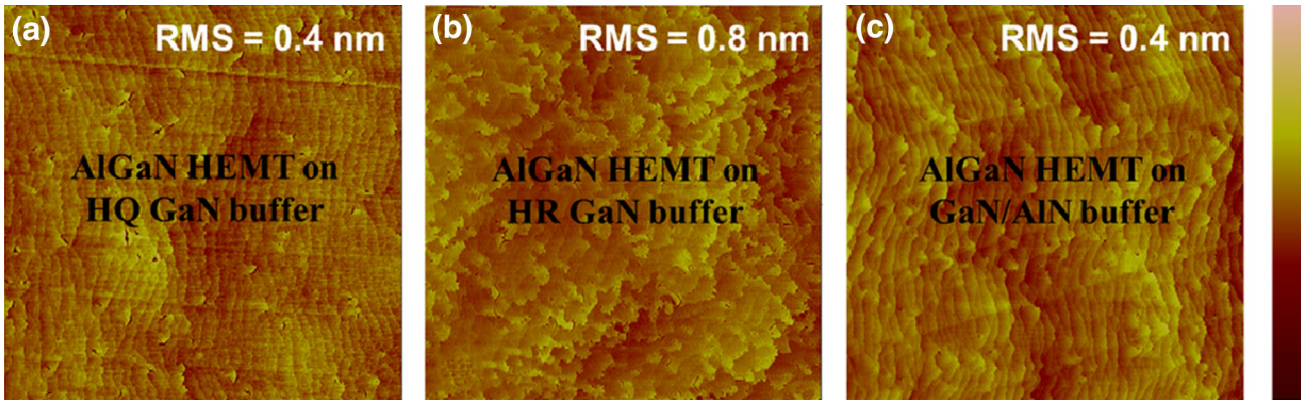


Fig. 5. Surface morphology of AlGaIn/GaN HEMTs using different buffer structures. All scans are $5 \mu\text{m} \times 5 \mu\text{m}$; vertical scale bars are 5 nm, 10 nm, and 5 nm for samples A to C, respectively (Color figure online).

two-dimensional electron gas (2DEG). Hall-effect measurements showed a sheet carrier concentration of $1.2 \times 10^{13} \text{ cm}^{-2}$ with Hall mobility of $1730 \text{ cm}^2/\text{V s}$, $1530 \text{ cm}^2/\text{V s}$, and $1820 \text{ cm}^2/\text{V s}$ for AlGaIn/GaN HEMTs grown on HQ GaN, HR GaN, and GaN/AlIn buffers, respectively. The higher electron mobilities for the HEMTs on the HQ GaN and GaN/AlIn buffers can in part be attributed to reduced fluctuation at the AlGaIn/GaN interface, as indicated by the reduced RMS roughness, and in part due to decreased defect density, as revealed by the narrowed XRD linewidth.

In addition to the channel resistivity, the breakdown characteristics are also of great importance for GaN-based transistors to take full advantage of their high current and power driving capabilities. To compare the breakdown characteristics of the different buffer structures on sapphire, the AlGaIn barrier and AlIn spacer layers were removed using Cl_2 -based ICP etching. Ti/Al/Ni/Au (20 nm/150 nm/50 nm/80 nm) electrodes separated by $100 \mu\text{m}$ were deposited by e-beam evaporation and annealed at 850°C in N_2 ambient. The buffer leakage current was measured versus applied voltage and is plotted in Fig. 6a. The two-terminal buffer breakdown voltage (V_{BV}) was defined as the measured voltage when the buffer leakage current reached $1 \mu\text{A}$. It

can be seen that the HQ GaN exhibited a poor V_{BV} of 11.5 V, while the HR GaN featured an enhanced V_{BV} exceeding 1000 V. These significantly improved breakdown characteristics are mainly attributed to the different growth mode shown in Fig. 6b. In the HQ GaN buffer growth, a 3D-to-2D transition growth mode was adopted to improve the crystalline quality while unintentional doping occurred during the prolonged 3D growth, introducing a leakage channel at the GaN-sapphire interface.^{13,14} With the 3D growth mode eliminated for the HR GaN buffer, significantly enhanced V_{BV} exceeding 1000 V could be achieved. The GaN/AlIn buffer also showed high V_{BV} over 1000 V, with leakage current level comparable to that of the HR GaN buffer.

To investigate this phenomenon, mercury C - V measurements were carried out on the AlGaIn/GaN heterostructures as illustrated in Fig. 7a, showing a sharp decrease of capacitance for all three samples with varied bias, indicating effective confinement of the carriers in the 2DEG channel. The minimum depletion capacitance (C_{min}) at high reverse bias of the AlGaIn/GaN HEMTs using the HQ GaN buffer was about one order of magnitude higher than for the HR GaN or GaN/AlIn buffer, which translates to an increased background concentration in the buffer layer (Fig. 7b). The HR buffer and GaN/AlIn buffer

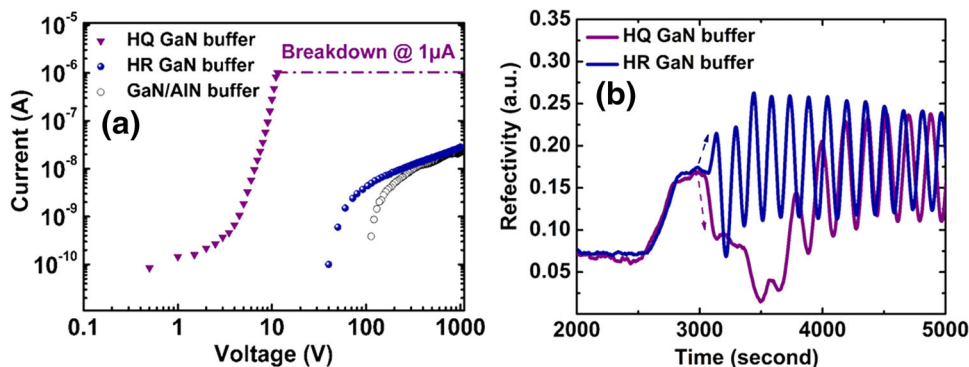


Fig. 6. (a) Leakage and breakdown characteristics of the three buffer structures. The two-terminal buffer breakdown voltage (V_{BV}) was defined as the measured voltage when the buffer leakage current reached $1 \mu\text{A}$. (b) *In situ* reflectance curves during HQ and HR GaN buffer growth (Color figure online).

both feature lower background concentration without any leakage channel underneath.

The crystalline quality of the as-grown HEMT samples was examined using a HRXRD system operating at voltage of 40 kV and current of 40 mA with Cu $K_{\alpha 1}$ radiation. The HRXRD omega rocking curves for (002) and (102) planes of the HEMT buffers are shown in Fig. 8a and b, respectively. The FWHM values from the HQ GaN buffer were 297 arcsec and 330 arcsec for (002) and (102) planes, respectively. Obvious broadening of the rocking curves can be seen for the HR GaN buffer, with FWHM values of 313 arcsec and 688 arcsec for (002) and (102) planes, respectively. This indicates an increased dislocation density of the HR GaN buffer, due to insufficient 3D island growth before quasi-2D growth. The GaN/AlN buffer exhibited FWHM values of 238 arcsec and 321 arcsec for (002) and (102) planes, respectively. The FWHM values can be related to the dislocation density through the following equations^{32,33}:

$$D_{\text{screw}} = \beta_{(002)}^2 / 9b_{\text{screw}}^2, \quad D_{\text{edge}} = \beta_{(102)}^2 / 9b_{\text{edge}}^2,$$

$$D_{\text{dislocation}} = D_{\text{screw}} + D_{\text{edge}}, \quad (1)$$

where D_{screw} is the screw dislocation density and D_{edge} is the edge dislocation density. $\beta_{(002)}$ and $\beta_{(102)}$ are the FWHM values in radians for the (002) and (102) omega rocking curves, respectively. The Burgers vector lengths b_{screw} and b_{edge} are 0.5185 nm and 0.3189 nm, respectively. The estimated dislocation density is $3.6 \times 10^8 \text{ cm}^{-2}$, $1.3 \times 10^9 \text{ cm}^{-2}$, and $3.2 \times 10^8 \text{ cm}^{-2}$ for the HQ GaN buffer, HR GaN buffer, and GaN/AlN buffer, respectively, similar to that reported in Ref. 34. It is noted that the dislocation density calculated from x-ray diffraction is at best a rough estimate; a more accurate dislocation density needs to be measured by transmission electron microscopy.³⁵ The superior crystalline quality of the GaN/AlN buffer can be attributed to the improved AlN under the optimal growth condition.

Afterwards, LED overgrowth was carried out on the exposed GaN buffers to verify the advantages of the GaN/AlN buffer for the LED part of the integrated HEMT-LED device. Nomarski optical micrographs of the LED epi grown on different buffers are shown in Fig. 9. All LED surfaces showed similar morphology with large density of dots, resulting from intentional surface roughening due to the lower growth temperature of the p -type layer. However, cracks were observed for the LED on the HR GaN buffer, while the LEDs grown on HQ GaN epi and GaN/AlN buffer were both crack free. This indicates that the LED epi grown on the HR GaN epi might be under tensile stress, inducing cracks. Furthermore, some semipolar facets can be observed in the vicinity of the cracks. It seems that the cracks occurred during the high-temperature GaN growth and were subsequently covered by additional material. The locally generated stress and the facets exposed by the cracks will induce a different growth mode, forming semipolar facets. The overall stress in an epitaxial GaN film on sapphire is a combined effect of the compressive strain induced by its thermal expansion mismatch compared with sapphire and the intrinsic tensile stress developed during 3D island coalescence.³⁶ Generally, the HQ GaN buffer grown on sapphire substrate is under thermal compressive stress after cooling down to room temperature. To achieve an HR GaN buffer on sapphire, the quasi-2D growth was carried out immediately after the low-temperature nucleation layer without annealing to diminish the 3D island density before coalescence. As a result, the increased island boundary not only degrades the crystalline quality but also leads to increased tensile stress during coalescence.³⁷ Tensile stress was further accumulated during subsequent n -type GaN growth of the LEDs.³⁸ As a result, the built-up tensile stress exceeded the thermal-mismatch-induced compressive stress and resulted in cracks during the LED epi growth. For the GaN/AlN buffer, the smaller lattice constant of the AlN layer will induce extra compressive strain in the

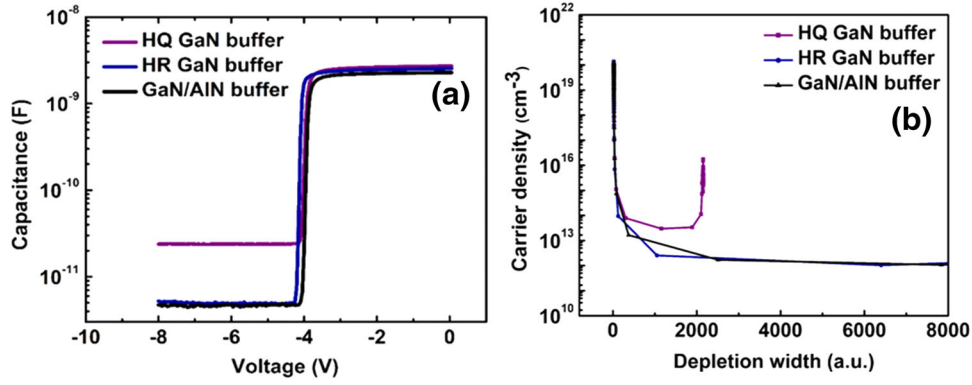


Fig. 7. (a) C - V characteristics and (b) carrier density profiles of AlGaIn/GaN heterostructures using different buffer structures (Color figure online).

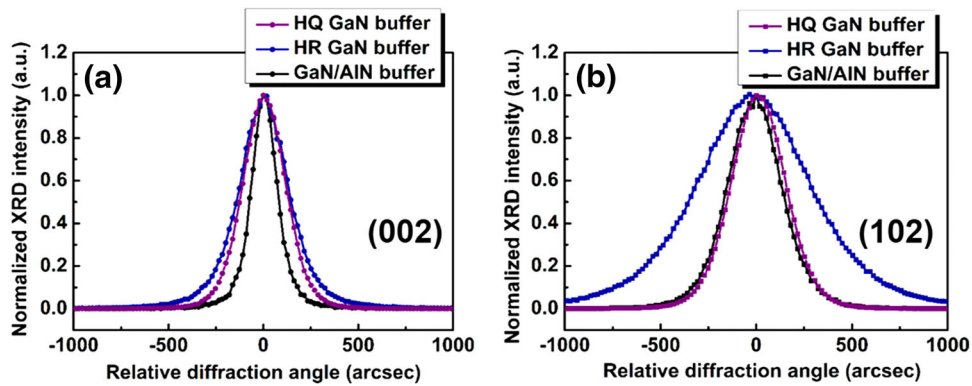


Fig. 8. (a) HRXRD (002) rocking curves and (b) HRXRD (102) rocking curves of the three buffer structures (Color figure online).

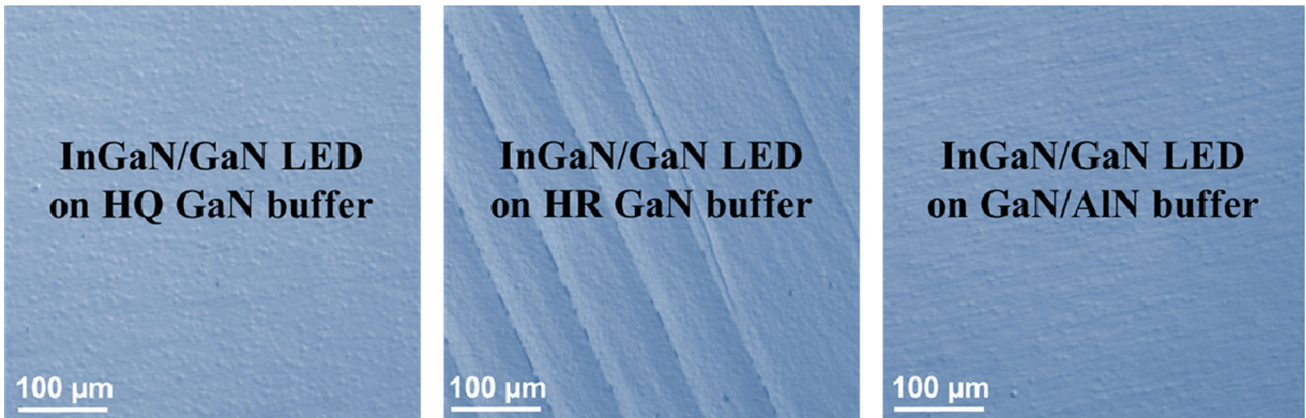


Fig. 9. Surface morphology of LED samples on different buffer structures under Nomarski interference optical microscopy.

upper GaN epi, which would compensate the tensile stress induced by SiH_4 doping and result in a crack-free LED.

Micro-Raman scattering spectroscopy was carried out at room temperature to further confirm the strain behaviors in the samples, as shown in Fig. 10a. Both GaN E_2 (TO) and A_1 (LO) phonon modes can be observed. The E_2 (TO) phonon is generally used to represent the residual stress state

in epitaxial layers. The residual in-plane biaxial stress $\sigma_{\chi\chi}$ can be estimated by

$$\sigma_{\chi\chi} = \Delta\omega/\kappa, \quad (2)$$

where $\Delta\omega$ is the strain-induced shift of the E_2 (TO) peak, while the Raman stress coefficient κ is $4.3 \text{ cm}^{-1}/\text{GPa}$ for the E_2 (TO) mode of GaN.³⁹ Compared with the stress-free GaN E_2 (TO) peak

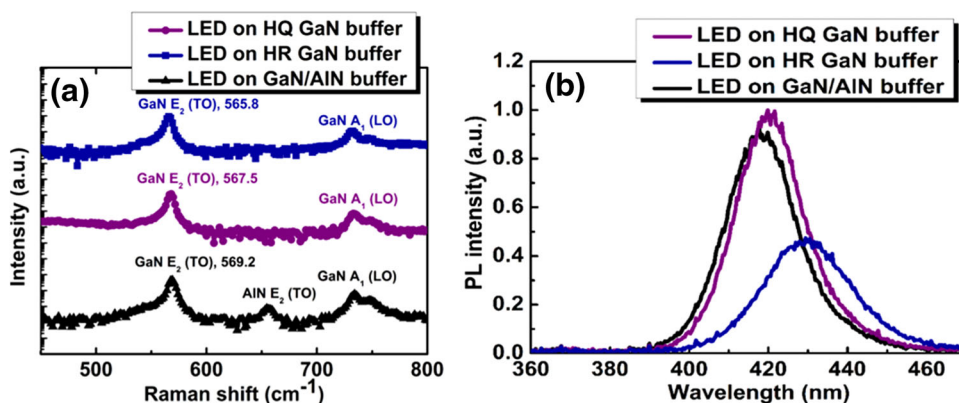


Fig. 10. (a) Micro-Raman and (b) PL spectra of LEDs with different buffer structures (Color figure online).

at 567.4 cm^{-1} ,⁴⁰ the LED grown on the HQ GaN buffer was nearly stress free, which is a combined result of the compressive strain due to thermal mismatch and tensile lattice stress from island coalescence. However, the E_2 (TO) peak for the LED on the HR GaN peak was blue-shifted to 565.8 cm^{-1} after cooling down to room temperature, corresponding to a tensile stress value of 0.372 GPa. Considering the large compressive stress introduced during cooling down (1.5 GPa),⁴¹ the GaN epi was under much higher tensile stress (exceeding 1.872 GPa) at the end of the high-temperature n -type GaN growth. This can explain the cracks formed during the high-temperature LED epi growth on the HR GaN buffer. The GaN/AlN buffer on sapphire showed a compressive strain value of 0.529 GPa, which is a combined effect of the smaller lattice of the AlN layer and the thermal mismatch between GaN and sapphire.

Room-temperature photoluminescence (PL) measurements were performed on the samples to explore the effect of the different buffers on the optical performance of the overgrown LEDs; the results are presented in Fig. 10b. It can be seen that the LEDs on the HQ GaN buffer and GaN/AlN buffer exhibited similar peak intensity, while the peak intensity of the LED on the HR GaN buffer was degraded by 53%, which can be attributed to either compromised crystalline quality or different light extraction efficiency. The FWHM values of the PL spectra were 19.9 nm, 20.6 nm, and 25.8 nm for the LEDs grown on the HQ GaN buffer, GaN/AlN buffer, and HR GaN buffer, respectively. The broadened linewidth of the PL spectrum is related to the degraded quality of the MQWs, which are impacted by the buffer layers beneath. Furthermore, due to the tensile stress from the bulk GaN buffer, the peak wavelength was red-shifted to 429 nm, compared with the LED grown on the HQ GaN buffer (419 nm). On the other hand, the blue-shift of the peak wavelength for the LED grown on the GaN/AlN buffer can also be attributed to the residual compressive strain from the GaN/AlN buffer.⁴²

Figure 11a illustrates the measured light-current (L - I) performance of discrete LEDs from the three samples with increasing injection current. The LEDs have a circular mesa with diameter of $300 \mu\text{m}$. Under injection current of 20 mA, the output power was 3.9 mW, 1.4 mW, and 4.0 mW for the LEDs on the HQ GaN buffer, HR GaN buffer, and GaN/AlN buffer, respectively. Moreover, the FWHM values from the electroluminescence (EL) spectra of the three samples were 19.9 nm, 19.8 nm, and 23.4 nm, respectively, which agrees with the linewidths of the PL spectra. The forward voltages of the three samples were 3.29 V, 3.31 V, and 3.26 V, respectively, as shown in Fig. 11b. For comparison purposes, the normalized efficiency against current density can be found in Fig. 11c. It can be seen that the peak efficiency of the LED on the GaN/AlN buffer was comparable to that on the HQ GaN buffer, while the LED on the HR GaN buffer featured a much lower efficiency, which was due to increased dislocation density from the HR buffer and thus degraded internal quantum efficiency from the active region. The reverse leakage current versus the bias voltage is also plotted in Fig. 11d. The reverse leakage current of the LED on the HR GaN buffer is one order of magnitude larger than that of the LEDs on the HQ GaN buffer and the GaN/AlN buffer. It is commonly known that the electrical properties, especially the reverse leakage current, are closely related to the crystalline quality of LED chips. This indicates that the HR GaN buffer will lead to inferior optical and electrical performance while the GaN/AlN buffer can provide LED performance comparable to the HQ GaN buffer.

Finally, integrated HEMT-LED devices were fabricated using the HR GaN buffer and the GaN/AlN buffer structure. The L - I curve of the integrated HEMT-LED is shown in Fig. 12. The size of the integrated LED is $450 \mu\text{m} \times 460 \mu\text{m}$, driven by a HEMT with W_g/L_g ratio of $475 \mu\text{m}/2 \mu\text{m}$ and drain-to-gate distance of $15 \mu\text{m}$. An injection current of around 100 mA can be achieved with V_{DD} increased to $\sim 8.4 \text{ V}$. The integrated HEMT-LED

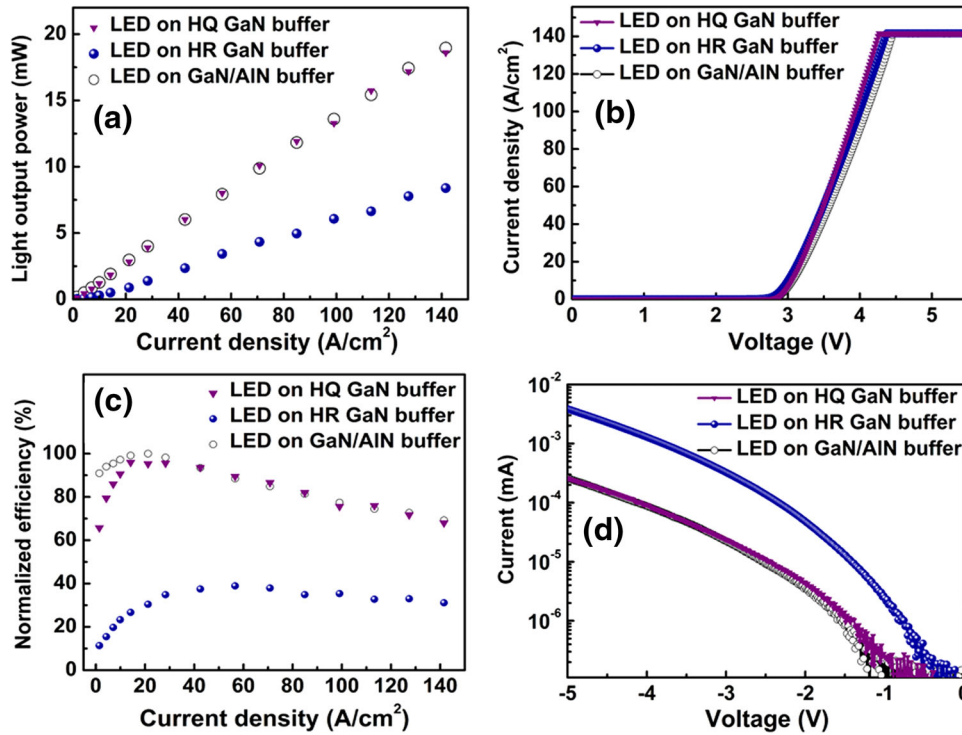


Fig. 11. (a) L - I curves, (b) I - V characteristics, (c) normalized efficiency against current density, and (d) reverse leakage current of discrete LEDs with different buffer structures.

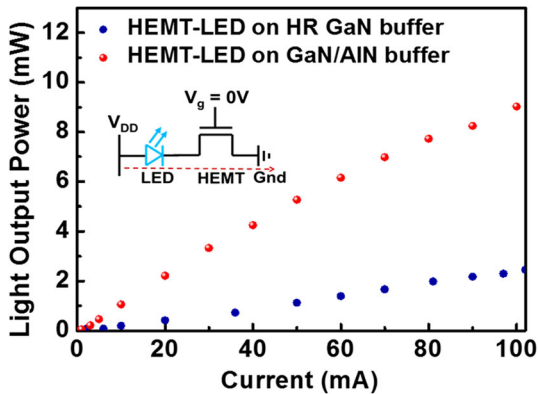


Fig. 12. L - I curves of integrated HEMT-LED devices using the HR GaN buffer and GaN/AlN buffer (Color figure online).

can emit light with integrated output power exceeding 9 mW, which is a dramatic increase compared with the integrated LED on the HR GaN buffer (~ 2.5 mW at injection current of 100 mA). The enhanced brightness of the integrated LED can be attributed to the superior crystalline quality of the GaN/AlN buffer, compared with the HR GaN buffer used in the previous report.⁹

CONCLUSIONS

The influence of different buffer structures on the performance of the HEMT and LED parts of monolithically integrated HEMT-LED devices has been

thoroughly investigated. A GaN/AlN buffer was developed, offering both high crystalline quality and superior breakdown characteristics. With the optimal GaN/AlN buffer, the integrated HEMT-LED device can emit an integrated light output power exceeding 9 mW at injection current of 100 mA, a significant improvement compared with the HEMT-LED fabricated on the HR GaN buffer. As a result, this GaN/AlN buffer structure can serve as a universal buffer for both the electrical and optical devices.

ACKNOWLEDGEMENTS

This work was supported in part by Grants 16204714 and T23-612/12-R from the Research Grants Council of Hong Kong. The authors would like to thank Jun Ma, Qiang Li, Clifford McAleese, Bei Shi, and Xinbo Zou for many helpful discussions, and Wilson Tang, as well as the staff of the MCPF & NFF of HKUST, for technical support.

REFERENCES

1. K.M. Lau, H.W. Choi, S.W.R. Lee, P.K.T. Mok, J.K.O. Sin, C.P. Yue, and W.H. Ki, *China Solid State Lighting* (China: Beijing, 2013).
2. Z. Li, J. Waldron, T. Detchprohm, C. Wetzel, R.F. Karlicek Jr., and T.P. Chow, *Appl. Phys. Lett.* 102, 192107 (2013).
3. Z. Li, J. Waldron, S. Chowdhury, L. Zhao, T. Detchprohm, C. Wetzel, R.F. Karlicek Jr., and T.P. Chow, *Phys. Status Solidi A* 212, 1110 (2015).
4. Y. Lee, Z. Yang, P. Chen, Y. Hsieh, Y. Yao, M. Liao, M. Lee, M. Wang, and J. Hwang, *Opt. Express* 22, 1589 (2014).
5. Z. Liu, T. Huang, J. Ma, C. Liu, and K.M. Lau, *IEEE Electron Device. Lett.* 35, 330 (2014).

6. Z. Liu, J. Ma, T. Huang, C. Liu, and K.M. Lau, *Appl. Phys. Lett.* 104, 091103 (2014).
7. C. Liu, Z. Liu, T. Huang, J. Ma, and K.M. Lau, *J. Cryst. Growth* 414, 243 (2015).
8. J. Waldron, R.F. Karlicek, and T.P. Chow, *Proceedings of International Workshop on Nitride Semiconductors*, Sapporo, Japan (2012).
9. C. Liu, Y. Cai, Z. Liu, J. Ma, and K.M. Lau, *Appl. Phys. Lett.* 106, 181110 (2015).
10. S. Nakamura, *Jpn. J. Appl. Phys.* 30, L1705 (1991).
11. J. Han, T.B. Ng, R.M. Biefeld, M.H. Crawford, and D.M. Follstaedt, *Appl. Phys. Lett.* 71, 3114 (1997).
12. D.D. Koleske, A.J. Fischer, A.A. Allerman, C.C. Mitchell, K.C. Cross, S.R. Kurtz, J.J. Figiel, K.W. Fullmer, and W.G. Breiland, *Appl. Phys. Lett.* 81, 1940 (2002).
13. S.D. Bakshi, J. Sumner, M.J. Kappers, and R.A. Oliver, *J. Cryst. Growth* 311, 232 (2009).
14. T. Zhu and R.A. Oliver, *Phys. Chem. Chem. Phys.* 14, 9558 (2012).
15. S. Heikman, S. Keller, S.P. DenBaars, and U.K. Mishra, *Appl. Phys. Lett.* 81, 439 (2002).
16. S. Heikman, S. Keller, T. Mates, S.P. DenBaars, and U.K. Mishra, *J. Cryst. Growth* 248, 513 (2003).
17. Y. Ohba and A. Hatano, *J. Cryst. Growth* 145, 214 (1994).
18. W. Götz, N.M. Johnson, J. Walker, D.P. Bour, and R.A. Street, *Appl. Phys. Lett.* 68, 667 (1996).
19. S.M. Hubbard, G. Zhao, D. Pavlidis, W. Sutton, and E. Cho, *J. Cryst. Growth* 284, 297 (2005).
20. H. Amano, N. Sawaki, I. Akasaki, and Y. Toyoda, *Appl. Phys. Lett.* 48, 353 (1986).
21. I. Akasaki, H. Amano, Y. Koide, K. Hiramatsu, and N. Sawaki, *J. Cryst. Growth* 98, 209 (1989).
22. J.N. Kuznia, M.A. Khan, D.T. Olson, R. Kaplan, and J. Freitas, *J. Appl. Phys.* 73, 4700 (1993).
23. K. Hiramatsu, S. Itoh, H. Amano, and I. Akasaki, *J. Cryst. Growth* 115, 628 (1991).
24. K. Okuno, T. Oshio, N. Shibata, Y. Honda, M. Yamaguchi, S. Tanaka, and H. Amano, *Phys. Status Solidi C* 10, 369 (2013).
25. O. Reentilä, F. Brunner, A. Knauer, A. Mogilatenko, W. Neumann, H. Protzmann, M. Heuken, M. Kneissl, M. Weyers, and G. Tränkle, *J. Cryst. Growth* 310, 4932 (2008).
26. V. Kueller, A. Knauer, F. Brunner, A. Mogilatenko, M. Kneissl, and M. Weyers, *Phys. Status Solidi C* 9, 496 (2012).
27. L.J. Ren, C. Liu, K.M. Lau, and J.K. O. Sin, *11th International Conference on Nitride Semiconductors*, Beijing, China (2015).
28. J. Jasinski, Z. Liliental-Weber, Q.S. Paduano, and D.W. Weyburne, *Appl. Phys. Lett.* 83, 2811 (2003).
29. Q.S. Paduano, D.W. Weyburne, J. Jasinski, and Z. Liliental-Weber, *J. Cryst. Growth* 261, 259 (2004).
30. M. Imura, N. Fujimoto, N. Okada, K. Balarishnan, M. Iwaya, S. Kamiyama, H. Amano, I. Akasaki, T. Noro, T. Takagi, and A. Bandoh, *J. Cryst. Growth* 300, 136 (2007).
31. X. Li, Y.O. Wei, S. Wang, H. Xie, T. Kao, M.M. Satter, S. Shen, P.D. Yoder, T. Detchprohna, R.D. Dupuis, A. Fischer, and F.A. Ponce, *J. Cryst. Growth* 414, 76 (2015).
32. R. Gay, P.B. Hirsch, and A. Kelly, *Acta Metall.* 1, 315 (1953).
33. T. Ide, M. Shimizu, X.Q. Shen, K. Jeganathan, H. Okumura, and T. Nemoto, *J. Cryst. Growth* 245, 15 (2002).
34. D. Zhu, C. McAleese, M. Häberlen, C. Salcianu, T. Thrush, M. Kappers, A. Phillips, P. Lane, M. Kane, D. Wallis, T. Martin, M. Astles, N. Hylton, P. Dawson, and C. Humphreys, *J. Appl. Phys.* 109, 014502 (2011).
35. M.A. Moram and M.E. Vickers, *Rep. Prog. Phys.* 72, 036502 (2009).
36. T. Böttcher, S. Einfeldt, S. Figge, R. Chierchia, H. Heinke, D. Hommel, and J.S. Speck, *Appl. Phys. Lett.* 78, 1976 (2001).
37. W.D. Nix and B.M. Clemens, *J. Mater. Res.* 14, 3467 (1999).
38. L.T. Romano, C.G. Van de Walle, J.W. Ager III, W. Götz, and R.S. Kern, *J. Appl. Phys.* 87, 7745 (2000).
39. B.H. Bairamov, O. Gürdal, A. Botchkarev, H. Morkoc, G. Irmer, and J. Monecke, *Phys. Rev. B* 60, 16741 (1999).
40. Y.V. Melnik, K.V. Vassilevski, I.P. Nikitina, A.I. Babanin, V. Yu Davydov, and V.A. Dmitriev, *MIJ-NSR* 2, e39 (1997).
41. J.D. Napierala, D. Martin, N. Grandjean, and M. Hegems, *J. Cryst. Growth* 289, 445 (2006).
42. M.E. Aumer, S.F. LeBoeuf, S.M. Bedair, M. Smith, J.Y. Lin, and H.X. Jiang, *Appl. Phys. Lett.* 77, 821 (2000).